Title
Mn2V2O7: An Earth Abundant Light Absorber for Solar Water Splitting

Journal
Advanced Energy Materials, 5(8)

ISSN
1614-6832

Authors
Yan, Qimin
Li, Guo
Newhouse, Paul F
et al.

Publication Date
2015-04-01

DOI
10.1002/aenm.201401840

Peer reviewed

$Mn_2V_2O_7$: An Earth Abundant Light Absorber for Solar Water Splitting

Qimin Yan, Guo Li, Paul F. Newhouse, Jie Yu, Kristin A. Persson, John M. Gregoire,* and Jeffrey B. Neaton**

As fossil fuels become increasingly depleted and expensive, effective use of solar energy has become an urgent task at the forefront of materials research. Among many different alternatives, the generation of chemical fuels offers a promising way to capture and store solar energy.[1,2] To deliver an efficient, integrated solar fuels device, new light-absorbing materials must be identified that meet stringent criteria with respect to bandgap, band edge energies, and electrochemical stability. For a solar water splitting device with a single light absorber, a bandgap in the range of 1.7–2.2 eV is desirable for capturing a sizeable fraction of solar radiation while providing sufficient photovoltage to drive water-splitting and other reactions.[3] For tandem light absorber designs, bandgaps in the range of 0.9–2.0 eV are of prime interest, as combining light absorbers from the low end and high end of this range can provide efficient capture of solar radiation and produce sufficient photovoltage.[4] For this tandem strategy, several *p*-type semiconductors such as Si, InP, and WSe_2 have been successfully demonstrated as the low-gap component material, further motivating the discovery of an *n*-type semiconductor with 1.6–2.0 eV gap. To perform photoelectrolysis, the conduction and valence bands of the single or tandem photoabsorber must also straddle the redox potentials of both the hydrogen evolution reaction (HER) [0 V vs the normal hydrogen electrode (NHE)] and oxygen evolution reaction (OER) (1.23 V vs NHE). Metal oxide semiconductors have been extensively researched for this application due to their chemical and electrochemical stability under oxidizing conditions, but the demanding set of requirements on band energetics has not been met by known metal oxides.[2]

Bandgaps of metal oxides are usually too large to absorb more than a small fraction of the solar spectrum, primarily because their valence band edges are usually derived from the oxygen 2*p* orbitals located at much higher potential (and lower electronic energy) than the H_2O/O_2 potential of 1.23 V versus NHE.[5] The large bandgap results in poor solar absorption efficiency, and this issue is compounded by the wasted photovoltage for water oxidation. Efforts have been made in the doping/codoping of currently available metal oxide photocatalysts (such as TiO_2[6] and $SrTiO_3$[7]), as well as in the fabrication of oxynitrides, to push the valence band maximum (VBM) to higher energy via hybridization between O 2*p* and N 2*p* states.[8] Unfortunately, the doping process can lead to recombination centers, dramatically decreasing the mobility of photogenerated carriers and limiting photocatalytic activity.[9] Incorporation of nitrogen, on the contrary, usually compromises the electrochemical stability of parent oxides.[10] To overcome the intrinsic limitations of currently available materials for photocatalytic and optoelectronic applications, it is highly desirable to develop new metal oxides with optimal bandgaps and band edge energies, motivating the exploration of ternary and higher order composition spaces.

In this work, we identify $Mn_2V_2O_7$ as a complex oxide exhibiting excellent optoelectronic properties with near-optimal bandgap and band alignment to the HER and OER standard potentials. With formal valences of Mn^{+2} and V^{+5}, $Mn_2V_2O_7$ is experimentally found to assume a distorted honeycomb structure, which exhibits a high-temperature phase (β-phase) and a low-temperature phase (α-phase).[11,12] In the β-phase, $Mn_2V_2O_7$ crystallizes in the monoclinic structure (space group C2/m) while in the α-phase, it adopts the triclinic structure (space group P1). At room temperature, $Mn_2V_2O_7$ is paramagnetic, with a paramagnetic-antiferromagnetic transition at $T = 16$ K.[11] The α–β phase transition temperature is close to room temperature ($T \approx 296$ K).[11] In this Communication, we focus on the high temperature phase β-$Mn_2V_2O_7$, which has recently been shown to grow readily at room temperature using a molten salt method.[12]

To understand the relevant structural, electronic, and magnetic properties of β-$Mn_2V_2O_7$, we perform spin-polarized first-principles calculations based on density functional theory (DFT) using the Vienna ab initio software package (VASP)[13] with the projector augmented wave (PAW) pseudopotentials;[14] the generalized gradient approximation (GGA) of Perdew,

Dr. Q. Yan, Dr. G. Li, Dr. J. Yu, Prof. J. B. Neaton
Molecular Foundry
Lawrence Berkeley National Laboratory
Berkeley, CA 94720, USA
E-mail: qiminyan@lbl.gov; jbneaton@lbl.gov
Dr. Q. Yan, Dr. G. Li, Dr. J. Yu, Prof. J. B. Neaton
Department of Physics
University of California Berkeley
Berkeley, CA 94720, USA
Dr. G. Li, Dr. J. Yu
Joint Center for Artificial Photosynthesis
Lawrence Berkeley National Laboratory
Berkeley, CA 94720, USA
Dr. P. F. Newhouse, Dr. J. M. Gregoire
Joint Center for Artificial Photosynthesis
California Institute of Technology
Pasadena, CA 91125, USA
E-mail: gregoire@caltech.edu
Dr. J. Yu, Dr. K. A. Persson
Environmental Energy Technologies Division
Lawrence Berkeley National Laboratory
Berkeley, CA 94720, USA
Prof. J. B. Neaton
Kavli Energy NanoSciences Institute
Berkeley, CA 94720, USA

DOI: 10.1002/aenm.201401840

Burke, and Ernzerhoff (PBE);[15] and the screened hybrid functional of Heyd, Scuseria, and Ernzerhoff (HSE).[16] A PBE + U approach is also used to address the on-site Coulomb interactions in the localized d orbitals through an additional Hubbard-type U term, with values of 4.0 eV for Mn and 3.1 eV for V as reported for isovalent binary metal oxides.[17] Within the HSE framework, the mixing parameter for the Hartree–Fock exchange potential is modified from 25% to 18%. Although formally, the generalized Kohn–Sham system associated with the HSE functional are rigorously not expected to yield quantitative bandgaps—as they are, in principle, lacking important exchange and correlation effects and electron-hole interactions[18]—this mixing parameter was selected so as to reproduce the experimental optical bandgap. (This small change in mixing parameter has relatively small effect on the lattice parameters and forces; all lattice optimizations reported here are performed with the mixing parameter set to 18%.) A $4 \times 4 \times 6$ Monkhorst–Pack k-point mesh for the integrations over the Brillouin zone of the conventional unit cell is used for all calculations. We carry out both bulk and surface relaxations until the forces on each atom are less than 0.01 eV $Å^{-1}$. We use an energy cutoff of 500 eV, and all calculations are spin-polarized. For our surface calculations, a 20 Å vacuum layer is used and sufficient.

The β-$Mn_2V_2O_7$ phase is a thortveitite-like structure composed of edge-sharing MnO_6 and staggered V_2O_7 bi-tetrahedra with a linear V–O–V configuration.[11] The low-temperature α-phase differs in that it exhibits bent X–O–X linkages (X = Mn, V) and a unit cell with lower symmetry and larger volume.[11] The β-$Mn_2V_2O_7$ primitive cell is shown in **Figure 1**. With C2/m symmetry, the thortveitite phase contains five unique lattice sites: Mn (4g), V (4i), O1 (2d), O2 (4i), and O3 (8j).[11] Our geometry relaxations with DFT-HSE lead to lattice parameters and Wyckoff positions in excellent agreement with experiment[11] (see **Table 1**). Each Mn atom is coordinated by a distorted oxygen octahedron, with nearest neighbor distances ranging from 2.09 to 2.28 Å, obtained from our structural optimization with DFT-HSE. Each V atom is at the center of a slightly distorted oxygen tetrahedron, with calculated V–O bond lengths ranging from 1.71 to 1.76 Å. The two VO_4 tetrahedra making up each V_2O_7 bitetrahedron exhibit a staggered conformation with a linear V–O–V configuration. We also carry out a comparison of different functionals and methods, including PBE, PBE + U, and HSE. We find that DFT-PBE underestimates the equilibrium lattice parameter *a* and overestimates *b* and *c* relative to experiment.[8] PBE + U improves upon PBE, and HSE leads to the best agreement with experiment (Table 1). A detailed discussion of our calculations of the electronic structure and magnetic properties appears in the Supporting Information.

Next, we turn to experiment and synthesize a bulk powder from a 1 mL aqueous solution containing 0.25 M each of $MnCl_2$ and VCl_3 and 15 vol% diethylene glycol. The stirred solution is placed in a crystallization dish and allowed to evaporate in a hood for 10 h to concentrate the metal salts. Approximately 50 µL of the concentrated precursor solution is pipetted into a ceramic micro crucible in a thermal gravimetric analysis (TGA) instrument (TA Instruments Q600), heated at 10 °C min^{-1} to 600 °C and held there for 1 h under 100 SCCM 20% O_2 in Ar. The resulting powder appears to have high optical absorption with a deep burgundy hue, and comparison of XRD measurements and simulated powder pattern reveals a primarily β-$Mn_2V_2O_7$ with a small fraction of α-$Mn_2V_2O_7$ (Figure S1, Supporting Information). The optically dense powder is characterized by diffuse reflectance spectroscopy using an integrating sphere (Model ISP-50–8-R-GT, Ocean Optics Inc), UV–vis illumination from a (200 W Newport Hg–Xe arc lamp) and a fiber coupled Spectral products SM 303. The spectral absorbance is calculated using the Kubelka–Munk radiative transfer model under the assumption of a wavelength-independent scattering factor, and the resulting Tauc plot for direct allowed bandgap analysis is shown in **Figure 2**a. For several repeat experiments and different variations of precursor chemistry and thermal processing, the extrapolated direct bandgap is consistently within 0.1–1.75 eV. The sample of Figure 2a exhibits a bandgap of approximately 1.8 eV, which places β-$Mn_2V_2O_7$ into the target bandgap range for high efficiency solar hydrogen generation.

Given this highly promising measured bandgap, we proceed to analyze the band structure of β-$Mn_2V_2O_7$ with DFT-HSE,

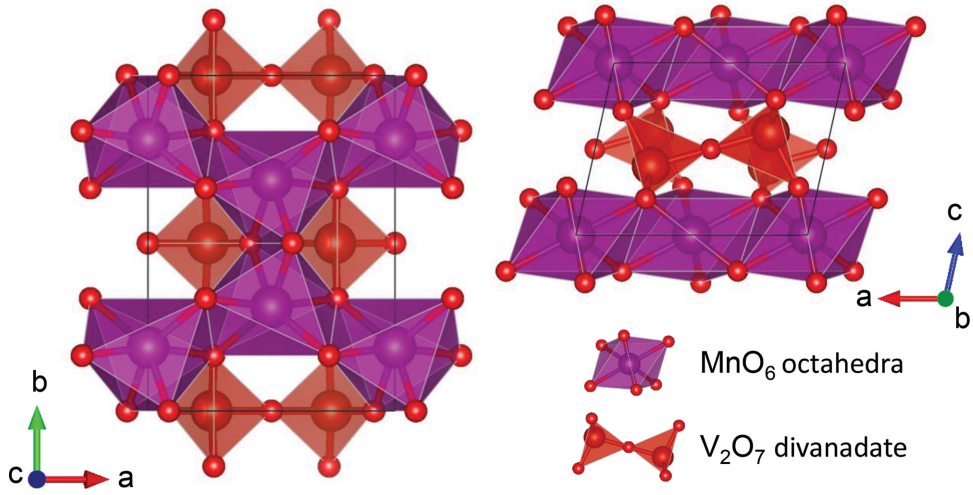

Figure 1. Structure of β-$Mn_2V_2O_7$. Blue: manganese; red: oxygen; and light pink: vanadium. The conventional unit cell is indicated by the black lines.

Table 1. Equilibrium lattice parameters, Wyckoff positions of atomic sites, and bandgaps of β-$Mn_2V_2O_7$ obtained from DFT-PBE, DFT-PBE + U, and DFT-HSE calculations. The experimental crystal structure data from ref. [11] and the experimentally measured bandgap from our present work are also listed for comparison.

		Expt.	Theory		
			PBE	PBE + U	HSE
a (Å)		6.713	6.566	6.429	6.625
b (Å)		8.725	8.954	8.759	8.729
c (Å)		4.969	5.087	5.067	4.983
β (deg)		103.591	102.197	102.201	103.257
Volume (Å^3)		282.88	292.34	278.87	280.50
Bandgap (eV)		1.75	0.82	1.20	1.73
Wyckoff position	Mn (4g)	(0, 0.8109, 0)	–	–	(0, 0.8114, 0)
	V (4i)	(0.7341, 0, 0.4032)	–	–	(0.7373, 0, 0.4012)
	O1 (2d)	(0.5, 0, 0.5)	–	–	(0.5, 0, 0.5)
	O2 (4i)	(0.9093, 0, 0.7191)	–	–	(0.9121, 0, 0.7188)
	O3 (8j)	(0.7322, 0.1614, 0.2123)	–	–	(0.7314, 0.1623, 0.2095)

adjusting the mixing parameter for the Hartree–Fock exchange potential to 0.18 to reproduce the experimental bandgap. Our calculated band structure appears in **Figure 3**a. β-$Mn_2V_2O_7$ is a near-direct bandgap insulator, with the VBM located at the *Z*-point, and the conduction band minimum (CBM) at *X*. The energy difference between the highest occupied states at *X* and *Z* is within 0.02 eV; hence, we describe the gap as near-direct. Via a simple fit of the energy–momentum dispersion along *I*–*X*, we predict effective masses of 0.81 and 1.34 m_0 for holes and electrons, respectively. The smaller hole-effective mass compared with that of electron reflects the strong hybridization between Mn *d* and O *p* states at the VBM. The site- and *l*-projected electronic densities of states (DOS) for β-$Mn_2V_2O_7$ are plotted in Figure 3b, and reveal a VBM composed of Mn 3*d* and O 2*p* states. The O 2*p* states spread between 0 and –5 eV relative to the VBM. The conduction band is dominated by V 3*d* states, with a small contribution from O 2*p* states. The absorption spectrum is obtained by calculating the dielectric matrix from the DFT-HSE Kohn–Sham spectrum, as shown in Figure 2b. At this approximate level of theory for the absorption spectrum, neglecting electron-hole interactions and assuming HSE provides a good description of the near-gap quasiparticle spectrum, we find good agreement with experiment; additionally, we predict fundamental band-edge transitions are dipole allowed, with direct absorption at the bandgap threshold.

To better understand the viability of $Mn_2V_2O_7$ for photocatalytic water splitting applications, we compute its band edge energies relative to vacuum, and discuss these energies relative to the redox potentials of water. Many-body perturbation theory with the GW approximation has been the method of choice in predicting band structures and band edge positions of semiconductors.[20–22] However, its application to complex systems is hampered by the high computational cost involved. Prior works have shown that DFT calculations with hybrid functionals can provide reliable and, in some cases, quantitative trends for band edge positions,[23–25] and excellent agreement with GW results has been reported for sp-bonded semiconductors and several oxides.[21,24] We compute bulk band edge positions relative to the vacuum level by combining our HSE bulk calculations and PBE + U surface slab calculations. In the bulk, the electronic eigenvalues are referenced to the average electrostatic potential (ionic plus Hartree). Following prior work,[22,25,26] our calculations are carried out in a supercell with a surface slab region and a vacuum region (**Figure 4**a). The vacuum level can be defined by the potential far away from the surface slab,

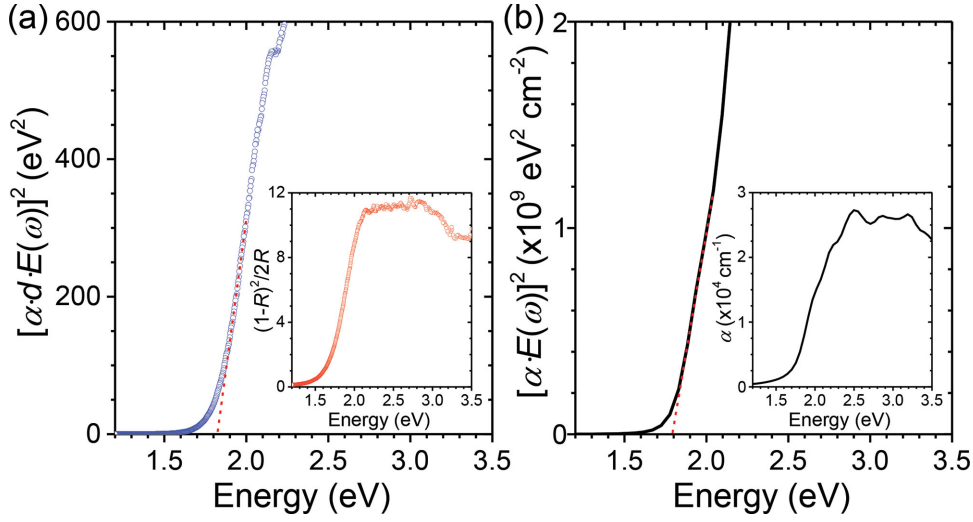

Figure 2. a) Tauc plot for direct allowed bandgap analysis. b) Calculated absorption spectrum of β-$Mn_2V_2O_7$ summed over all possible direct valence-to-conduction band transitions and averaged along three principle directions.

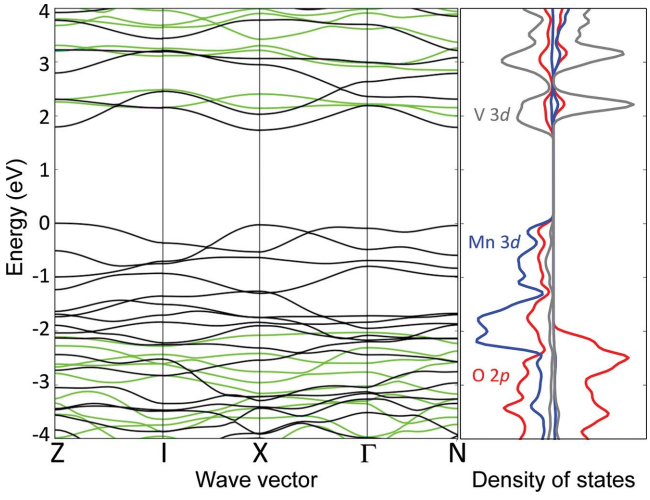

Figure 3. a) Band structure; and b) site- and *l*-projected electronic DOS of β-$Mn_2V_2O_7$. The highest occupied state is set to 0 eV. Notations for high-symmetry k-points are defined in ref. [19]. The electronic bands in the spin-up and spin-down channels are in black and green, respectively.

and the "bulk" average electrostatic potential is defined as the macroscopically averaged electrostatic potential taken from the "bulk" region deep inside the slab. In this manner, we establish the potential step ΔV between the vacuum and the bulk (Figure 4b), and the bulk electronic eigenvalues can be referenced to the vacuum. This approach has been used to evaluate the band alignment in traditional nitride semiconductors, resulting in good agreement with experiment.[25]

Note that our computed ΔV is surface orientation- and termination-dependent. Previous work has shown that the lowest energy surface orientations and terminations are most relevant for the position of the band edges.[25] Using the surface generation scheme proposed in ref. [27], we construct several low-index nonpolar surfaces of β-$Mn_2V_2O_7$, carry out surface geometry optimization, and calculated their surface energies. The (110) surface is found to have the lowest energy. This finding is consistent with the experimental observation that the (110) plane is the dominant crystal surface for β-$Mn_2V_2O_7$.[12] From our calculations, we find that the CBM is located at 4.68 eV below the vacuum and the VBM is at 6.41 eV below the vacuum.

In aqueous solution, an additional shift of these band edge energies (relative to the water redox levels) is expected from charge rearrangement and the formation of new species associated with the solution-semiconductor interface. This interface dipole depends on the nature of the surface and is intrinsic to β-$Mn_2V_2O_7$. First-principles prediction of this effect requires explicit treatment of a semiconductor-water interface,[28–30] which is beyond the scope of this work. Studies of several related oxides in ref. [22] has shown that the interface dipole can be approximated by a 0.5 eV upward shift of the VBM/CBM closer to vacuum at the point of zero charge (PZC), where the PZC corresponds to the pH value for which the surface is charge neutral.[31] While the corresponding pH of the PZC is unknown, the pH of PZC for a related compound, $BiVO_4$, is experimentally measured to be close to 2.5 ≈3.[32] Assuming the PZC of $Mn_2V_2O_7$ is close to that of $BiVO_4$, and estimating the potential shift from the Nernst equation (59 meV shift closer to vacuum per unit of pH), the band edge positions in aqueous solution at pH = 0 are estimated to be ≈0.35 eV closer to vacuum than predicted by our DFT calculations alone. This additional shift will locate the CBM at 4.33 eV below the vacuum and the VBM at 6.06 eV below the vacuum. As shown in Figure 4c, these CBM and VBM values straddle the two water redox potentials in a near-optimal fashion. Considering the uncertainty in the estimated potential shift in solution, variations in surface potential drop among different surface orientations/terminations (≈0.25 eV), and the fact that our bandgap is also approximate, we set an error bar of –0.3–0.25 eV for the CBM, and –0.4–0.15 eV for the VBM, respectively, for the predicted band edges.

To understand the underlying chemistry that gives rise to the excellent bandgap and band edges for water splitting, we further discuss its electronic structure. The stoichiometry of the system indicates that the formal oxidation states are +2, +5, and –2 for Mn ($3d^5$), V ($3d^0$), and O ($2p^6$), respectively. Each constituent Mn atom is predicted to be in a high-spin d^5 configuration, with a calculated magnetic moment of 4.58 μ_B (DFT-HSE). The occupied Mn 3*d* states are located at higher energies relative to the O 2*p* states. The hybridization between Mn 3*d* states and O 2*p* states provides considerable valence band dispersion. Due to the large exchange splitting, the unoccupied Mn 3*d* states in the other spin channel are higher in energy than the unoccupied V 3*d* states. For comparison, a well-studied photocatalytic light absorber, monoclinic $BiVO_4$, possesses a bandgap near 2.4 eV, and also features a CBM consisting mainly of V 3*d* states.[33,34] The valence band of $BiVO_4$; however, has primarily O 2*p* character, leading to a deep valence band with electrochemical potential in excess of 2.5 V versus NHE.[34] In contrast to $BiVO_4$, the presence of Mn 3*d* occupied

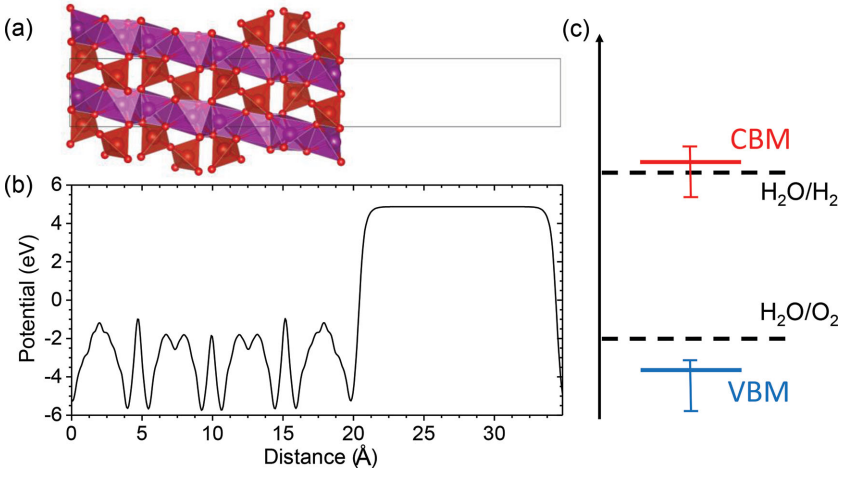

Figure 4. a) The slab model of β-$Mn_2V_2O_7$ (001) surface. b) Planar averaged electrostatic potential. c) Estimated CBM and VBM positions in aqueous solution relative to the two water redox potentials.

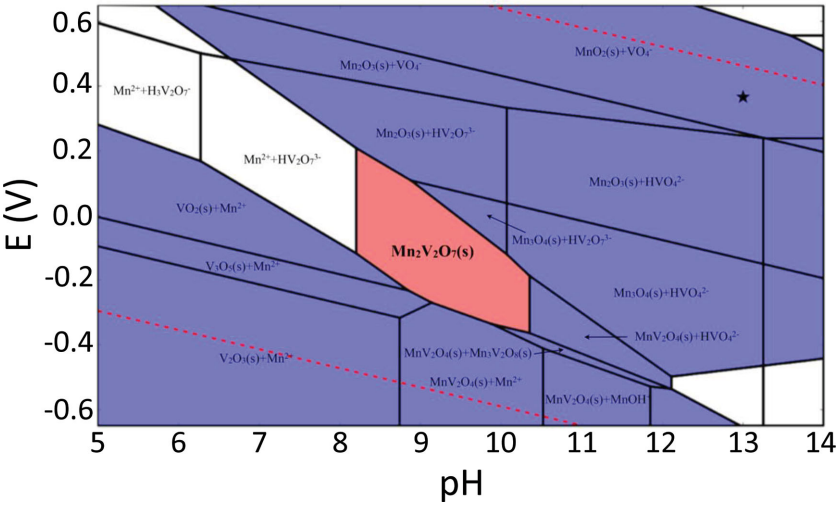

Figure 5. The Pourbaix diagram of the M–V–O system, assuming Mn- and V-ion concentrations of 10^{-4} mol kg^{-1}.

states in β-$Mn_2V_2O_7$ brings the VBM closer to the OER redox potential and results in the much smaller, more desirable bandgap.

A critical issue prohibiting the application of many candidate materials for water splitting is stability against photocorrosion. To explore this further, we compute Pourbaix diagrams, where solid and dissolved species are combined in a single phase diagram to determine the stable species (solids and/or aqueous ions) as a function of pH and potential.[35] In construction of our Pourbaix diagrams, DFT-PBE + U is used for the total energies of the solid phases, and experimental data are used for those of the dissolved ions, following previous work.[36] Our calculations suggest that, if the concentrations of Mn and V ions are very low at ≈10^{-6} mol kg^{-1}, β-$Mn_2V_2O_7$ is thermodynamically unstable with respect to Mn^{2+} and VO_3^- ions. However, when corresponding ion concentrations are higher than 10^{-4} mol kg^{-1}, the normalized Gibbs free energy of β-$Mn_2V_2O_7$ becomes lower than all the possible dissolution products, and it can exist in aqueous solutions as a solid. The calculated Pourbaix diagram in **Figure 5** assumes a Mn-ion concentration at 10^{-4} mol kg^{-1} and a V-ion concentration at 10^{-4} mol kg^{-1}. In this diagram, β-$Mn_2V_2O_7$ is stable in aqueous solution in mild base over an approximately 0.3 V window between the water redox potentials, and we note that this semiconductor may exhibit kinetic stability beyond these conditions.

To further assess the photocatalytic performance of this compound, a $Mn_{0.5}V_{0.5}O_x$ sample from a combinatorial composition library was prepared on an SnO_2:F conducting substrate using a similar metal precursor mixture and calcination as the powder sample described above, yielding a film with small pores as shown in **Figure 6**. The sample was characterized using a previously described scanning drop cell[37] to measure the photocurrent under chopped 385-nm illumination in 0.1 M NaOH (aq) with 5×10^{-2} M $[Fe(CN)_6]^{3-/4-}$ redox couple. The back contact of the samples was shorted to a Pt counter electrode and the short-circuit current was measured with the solution poised at the redox couple potential of 0.36 V versus NHE, which is approximately 0.1 V below the oxygen evolution potential in the pH 13 solution (marked by a black star in Figure 5). The last 20 of a 44 s experiment with 1 Hz illumination is shown in Figure 6, showing stable photocurrent in excess of 0.1 mA cm^{-2}. We note that due to shunted current in the electrochemical cell, which is common for photoelectrochemistry of a facile redox couple, this experiment provides a semiquantitative measure of photoactivity but not a photon-to-current conversion efficiency. The positive photocurrent indicates n-type photoactivity in which photogenerated holes in the $Mn_{0.5}V_{0.5}O_x$ sample were transferred to solution to oxidize the dissolved ferrocyanide. Repeating the measurement on a duplicate sample with 0.1 M NaOH (aq) and without the facile redox couple yielded no measureable photocurrent. The first measurement is commensurate with conduction and valence bands straddling the redox couple potential, and the latter measurement indicates that the metal oxide is not a good photocatalyst, which is most likely due to the valence band offset of approximately 0.3 V, which is only sufficient over potential to catalyze oxygen evolution with optimized catalysts. The stable photocurrent in the former measurement and lack of photocurrent in the latter also indicate that the $Mn_{0.5}V_{0.5}O_x$ sample does not appreciably photocorrode under these conditions. Further experiments are required to ascertain the kinetic stability and its relation to the calculated thermodynamics of Figure 5. Overall, these photocurrent results corroborate the excellent calculated optoelectronic properties and suggest that when coupled with an appropriate oxygen evolution electrocatalyst, electronic quality β-$Mn_2V_2O_7$ has the potential to enable very efficient photo-driven water splitting. The combined properties of valence band alignment for OER, sub-2 eV bandgap and stability under illumination in pH 13 make this light absorber truly unique, and a comparison with other semiconductors is provided in the Supporting

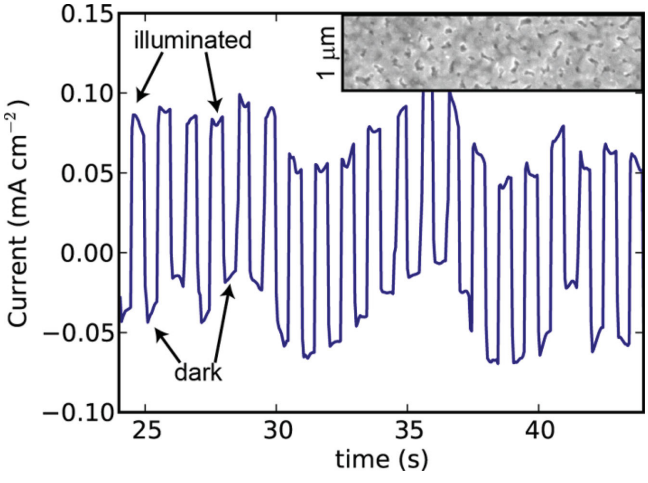

Figure 6. Final 20 of a 44 s short-circuit photocurrent with 1 Hz chopped illumination. The inset shows a 1 × 4 μm SEM view of the $Mn_{0.5}V_{0.5}O_x$ sample. The drifting dark current is typical of short-circuit measurements with a facile redox couple.

Information. Combinatorial experiments are underway to measure photoelectrochemical properties and phase behavior of the Mn–V oxide composition space, and will be presented in a future publication.

In summary, we present the joint computational and experimental identification of $Mn_2V_2O_7$ as a highly promising light absorber for photocatalytic water splitting. Our calculations suggest that this system has a desirable bandgap, and a synthesized powder indeed leads to a gap of 1.75 (±0.1) eV, in the desired range for an optimal solar photoanode. From DFT-HSE and DFT-PBE + U electronic structure calculations, β-$Mn_2V_2O_7$ is also found to possess a near-optimal band alignment to the HER and OER redox potentials. This stems from a strong hybridization of Mn 3*d* and O 2*p* states to form a VBM closer to the OER potential than typical metal oxide semiconductors, and the V 3*d* character of the conduction band leads to a CBM close to the HER potential. Experiments further indicate appreciable photocurrent from β-$Mn_2V_2O_7$ samples under specific electrochemical conditions, indirectly corroborating our predictions. Our study demonstrates and clarifies the unique role played by each element in the structural and functional electronic properties of β-$Mn_2V_2O_7$. The results and detailed understanding of this material provide a path toward the design of additional metal oxide light absorbers with desirable band energetics for solar fuels applications.

Supporting Information

Supporting Information is available from the Wiley Online Library or from the author.

Acknowledgements

Computational work was supported by the Materials Project Predictive Modeling Center (EDCBEE) through the U.S. Department of Energy, Office of Basic Energy Sciences, Materials Sciences and Engineering Division, under Contract No. DE-AC02–05CH11231. Experimental work was performed by the Joint Center for Artificial Photosynthesis, a DOE Energy Innovation Hub, supported through the Office of Science of the U.S. Department of Energy (Award No. DE-SC0004993). Work at the Molecular Foundry was supported by the Office of Science, Office of Basic Energy Sciences, of the U.S. Department of Energy under Contract No. DE-AC02–05CH11231. Computational resources also provided by the Department of Energy through the National Energy Supercomputing Center. The authors thank Dan Guevarra and Aniketa Shinde for assistance with acquisition of the photocurrent data and Chengxiang Xiang, Slobodan Mitrovic and Joel Haber for helpful discussions.

Received: October 17, 2014
Revised: November 27, 2014
Published online:

[1] A. Fujishima, K. Honda, *Nature* **1972**, *238*, 37.
[2] F. E. Osterloh, *Chem. Mater* **2008**, *20*, 35.
[3] M. G. Walter, E. L. Warren, J. R. McKone, S. W. Boettcher, Q. Mi, E. A. Santori, N. S. Lewis, *Chem. Rev.* **2010**, *110*, 6446.
[4] S. Hu, C. Xiang, S. Haussener, A. D. Berger, N. S. Lewis, *Energy Environ. Sci.* **2013**, *6*, 2984.
[5] K. Maeda, K. Domen, *J. Phys. Chem. C* **2007**, *111*, 7851.
[6] W. J. Yin, H. W. Tang, S. H. Wei, M. M. Al-Jassim, J. Turner, Y. F. Yan, *Phys. Rev. B* **2010**, *82*, 045106.
[7] K. M. K. Sayama, R. Abe, Y. Abe, H. Arakawa, *Chem. Commun.* **2001**, *23*, 2416.
[8] G. Hitoki, T. Takata, J. N. Kondo, M. Hara, H. Kobayashi, K. Domen, *Chem. Commun.* **2002**, 1698.
[9] W. Y. Choi, A. Termin, M. R. Hoffmann, *J. Phys. Chem.* **1994**, *98*, 13669.
[10] I. E. Castelli, K. S. Thygesen, K. W. Jacobsen, *Top. Catal.* **2014**, *57*, 265.
[11] J. H. Liao, F. Leroux, C. Payen, D. Guyomard, Y. Piffard, *J. Solid State Chem.* **1996**, *121*, 214.
[12] C. C. Zhou, F. M. Liu, P. Ding, *Chin. Phys. B* **2009**, *18*, 5055.
[13] G. Kresse, J. Furthmuller, *Comput. Mater. Sci* **1996**, *6*, 15.
[14] P. E. Blochl, *Phys. Rev. B* **1994**, *50*, 17953.
[15] J. P. Perdew, K. Burke, M. Ernzerhof, *Phys. Rev. Lett.* **1996**, *77*, 3865.
[16] a) J. Heyd, G. E. Scuseria, M. Ernzerhof, *J. Chem. Phys.* **2003**, *118*, 8207; b) J. Heyd, G. E. Scuseria, M. Ernzerhof, *J. Chem. Phys.* **2006**, *124*, 219906.
[17] L. Wang, T. Maxisch, G. Ceder, *Phys. Rev. B.* **2006**, *73*, 195107.
[18] S. Kummel, L. Kronik, *Rev. Mod. Phys.* **2008**, *80*, 3.
[19] W. Setyawan, S. Curtarolo, *Comput. Mater. Sci.* **2010**, *49*, 299.
[20] a) R. Shaltaf, G. M. Rignanese, X. Gonze, F. Giustino, A. Pasquarello, *Phys. Rev. Lett.* **2008**, *100*, 186401; b) V. Stevanovic, K. Hartman, R. Jaramillo, S. Ramanathan, T. Buonassisi, P. Graf, *Appl. Phys. Lett.* **2014**, *104*, 211603.
[21] W. Chen, A. Pasquarello, *Phys. Rev. B* **2012**, *86*, 035134.
[22] V. Stevanovic, S. Lany, D. S. Ginley, W. Tumas, A. Zunger, *Phys. Chem. Chem. Phys.* **2014**, *16*, 3706.
[23] a) A. Wadehra, J. W. Nicklas, J. W. Wilkins, *Appl. Phys. Lett.* **2010**, *97*, 092119; b) H. P. Komsa, P. Broqvist, A. Pasquarello, *Phys. Rev. B* **2010**, *81*, 205118.
[24] A. Alkauskas, P. Broqvist, F. Devynck, A. Pasquarello, *Phys. Rev. Lett.* **2008**, *101*, 106802.
[25] P. G. Moses, M. S. Miao, Q. M. Yan, C. G. Van de Walle, *J. Chem. Phys.* **2011**, *134*, 084703.
[26] Y. Ping, G. Galli, *J. Phys. Chem. C* **2014**, *118*, 6019.
[27] W. H. Sun, G. Ceder, *Surf. Sci.* **2013**, *617*, 53.
[28] N. Kharche, J. T. Muckerman, M. S. Hybertsen, *Phys. Rev. Lett.* **2014**, *113*, 176802.
[29] T. A. Pham, D. Lee, E. Schwegler, G. Galli, *J. Am. Chem. Soc.* **2014**, *136*, 17071.
[30] Y. Wu, M. K. Y. Chan, G. Ceder, *Phys. Rev. B* **2011**, *83*, 235301.
[31] M. A. Butler, D. S. Ginley, *J. Electrochem. Soc.* **1978**, *125*, 228.
[32] a) A. H. Abdullah, H. J. M. Moey, N. A. Yusof, *J. Environ. Sci. (China)* **2012**, *24*, 1694; b) N. C. Castillo, A. Heel, T. Graule, C. Pulgarin, *Appl. Catal. B: Environ.* **2010**, *95*, 335.
[33] A. Kudo, K. Omori, H. Kato, *J. Am. Chem. Soc.* **1999**, *121*, 11459.
[34] A. Walsh, Y. Yan, M. N. Huda, M. M. Al-Jassim, S. H. Wei, *Chem. Mater.* **2009**, *21*, 547.
[35] M. Pourbaix, *Atlas of Electrochemical Equilibria in Aqueous Solutions*, National Association of Corrosion Engineers, Houston, TX **1974**.
[36] K. A. Persson, B. Waldwick, P. Lazic, G. Ceder, *Phys. Rev. B* **2012**, *85*, 235438.
[37] J. M. Gregoire, C. X. Xiang, X. N. Liu, M. Marcin, J. Jin, *Rev. Sci. Instrum.* **2013**, *84*, 024102.